ADVANCED MATERIALS
www.advmat.de

Anatomy of a Nanoscale Conduction Channel Reveals the Mechanism of a High-Performance Memristor

Feng Miao, John Paul Strachan, J. Joshua Yang, Min-Xian Zhang, Ilan Goldfarb, Antonio C. Torrezan, Peter Eschbach, Ronald D. Kelley, Gilberto Medeiros-Ribeiro, and R. Stanley Williams**

Present memory technologies, including DRAM (dynamic random access memory), SRAM (static random access memory), and flash, are potentially approaching their scalability limits near the 16 nm technology generation.[1–3] Accordingly, the International Technology Roadmap for Semiconductors (ITRS) has recently completed an assessment of eight memory technologies among the emerging research devices (ERDs) and recommended that Redox RAM[4–7] and STT-MRAM[8,9] (spin-transfer torque magnetic RAM) receive additional focus in research and development.[1] Redox RAM is one type of memristor[10–15] that has shown more than adequate scalability, non-volatility, multiple-state operation, 3D stackability, and complementary metal-oxide semiconductor (CMOS) compatibility.[16–39] Moreover, these devices have also exhibited significant potential in other applications, such as stateful logic operations,[40] neuromorphic computing,[27,41] and CMOS/memristor hybrid circuits for configuration bits and signal routing.[42] However, as pointed out by the ITRS 2010, there are still challenges remaining for these devices, among which are reliability and a better understanding of the microscopic picture of the switching.[1] The reliability issue includes switching endurance, long-term thermal stability, repeatability, and robustness of the conduction channel,[1] all of which depend on the chemical and structural details of the conduction channel revealed in this study.

Significant progress has been made in device performance using tantalum oxide based memristors. We recently demonstrated over 10^{10} open-loop switching cycles[43] in tantalum oxide based devices, with the device remaining switchable after 15 billion cycles without any feedback or power-limiting circuits.[43,44] This endurance record was surpassed within a year to 10^{12} by Lee et al.,[45] also using a tantalum oxide system. In addition, switching in less than 2 ns is demonstrated in **Figure 1**a, using a relatively low voltage (<2 V) for switching both ON (set) and OFF (reset). The as-prepared device was activated into normal switching operation by a 5 ns pulse with the same ON switching voltage utilized in the subsequent switching cycles (inset to Figure 1a), and so no high voltage or long-time electroforming was required. Favorable device size scaling is demonstrated in Figure 1b,c, in which crossbar nanodevices with 50 nm half-pitch (device size and also the distance between two neighboring devices) show less than 10 A switching current, which is encouraging for low-energy device applications. These promising device characteristics highlight the importance of understanding both the structure and switching mechanism of tantalum oxide based devices in order to engineer further improvements.

Switching mechanisms in many transition metal oxide based resistance switches[5,6,13,46] have been extensively studied, and the drift/diffusion of oxygen vacancies[47] (or anions) driven by an electric field and/or thermochemical reduction/oxidation[48] are believed to play a key role. Lee et al.[45,49] have adopted a drift switching mechanism similar to that introduced for TiO_2 memristive switching[13] to explain tantalum oxide based devices. However, there are strong qualitative differences[43] in the switching observed between Ti-O and Ta-O systems, suggesting major differences in the mechanism that should be observable. Thus, it is crucial to identify and image the actual "active" switching region buried inside the device since electrical operation, especially any electroforming process (used in ref. [45]), can significantly change the as-fabricated structure and material composition. This has been a longstanding desire since the 1960s[4,50,51] and important progress has been made recently.[46,52,53] For example, a crystalline sub-oxide has been identified as the conduction channel in both unipolar and bipolar TiO_2-based switches.[46,54] One approach is to prepare and examine a large number of sample slices through a device that has been switched in order to find one with filament-like features. This technique is time-consuming and cannot guarantee success in finding "the" active conduction channel responsible for the switching behavior observed in a device before it is destroyed. Here, we implemented a method for locating the nanoscale channel responsible for bipolar switching in a $Pt/TaO_x/Ta$ memristor. A microscopic picture of the conduction channel was then obtained, which was different from that observed for Ti-O and significantly constrained the possible switching mechanism of the tantalum oxide system. We propose a new switching mechanism for the tantalum oxide memristor system that is consistent with both the structure of the conduction channel and the observed electrical properties of the device.

As shown in **Figure 2**, the method we employed for finding and characterizing the active conduction channels

Dr. F. Miao, Dr. J. P. Strachan, Dr. J. J. Yang, Dr. M.-X. Zhang, Prof. I. Goldfarb,[+] Dr. A. C. Torrezan, Dr. G. Medeiros-Ribeiro, Dr. R. S. Williams
Hewlett-Packard Laboratories
1501 Page Mill Rd., Palo Alto, CA 94304, USA
E-mail: jianhuay@hp.com; stan.williams@hp.com
Dr. P. Eschbach, R. D. Kelley
Hewlett-Packard, 1000 NE Circle Blvd., Corvallis, OR 97330, USA
[+] Present address: Faculty of Engineering, Tel Aviv University, Tel Aviv 69978, Israel

DOI: 10.1002/adma.201103379

© 2011 WILEY-VCH Verlag GmbH & Co. KGaA, Weinheim

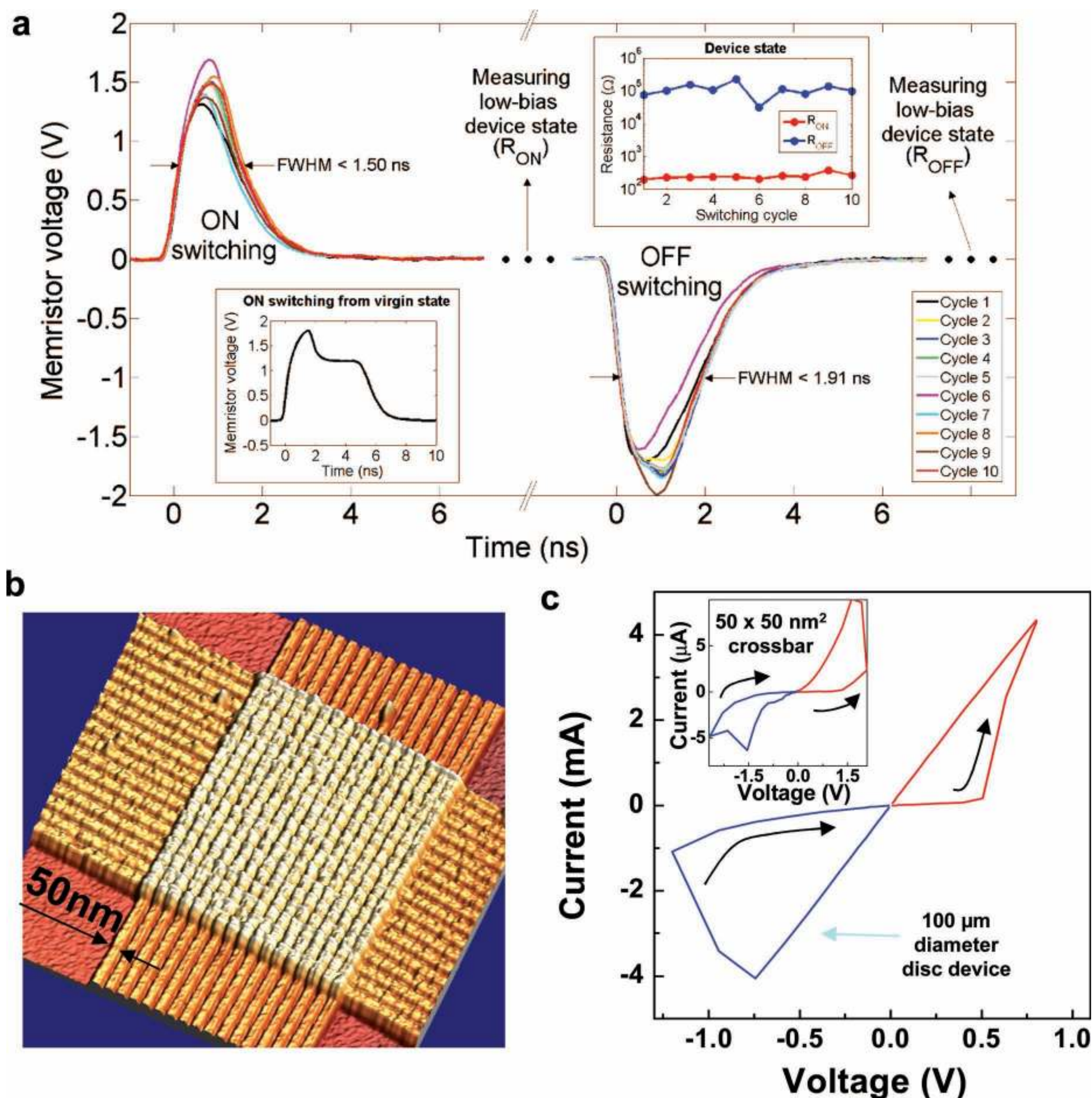

Figure 1. Electrical performance of tantalum oxide based memristors. a) Repeatable high speed switching under 2 ns measured in real-time for ON and OFF switching with a less than 2 V pulse (showing ten voltage–time curves for each). No significant electroforming is required: lower left inset shows the first ON switching, which activated the as-prepared device into a switchable state using a 5 ns, <2 V pulse. Upper right inset shows the reproducibility of the resistance values for the first ten ON and OFF pulses. b) 17 × 17 memristor cross bar with 50 nm half pitch. c) Current–voltage curves from a 100 m diameter disc device and a 50 nm half-pitch crosspoint device (inset), showing the fabrication scalability and decreasing current level with decreasing device size.

consisted of three steps: i) precisely locating the active switching region(s) through pressure-modulated conductance microscopy (PMCM)[55] on a functioning device; ii) cross-sectioning the active switching region(s) by focused ion beam (FIB) milling; and iii) examining the structure and composition through high-resolution cross-sectional transmission electron microscopy (X-TEM) and electron-energy-loss spectroscopy (EELS).

The PMCM procedure is schematically shown in Figure 2a. We used a non-conducting atomic force microscopy (AFM) tip to apply pressure to the top electrode of a cross-bar device and simultaneously monitored the change of resistance of the device at a small current bias, yielding a resistance map as a function of tip position. When the tip pressurized an active region in which the flow of current was dominant, a resistance dip appeared on resistance maps, originating from the compression of the conduction channel[56] or decrease of the tunneling or hopping distance.[55,57] By correlating the resistance map with the AFM topography image collected simultaneously, we were able to locate the position of the buried active switching region with a lateral resolution determined by the radius of the AFM tip (≈10 nm). Figure 2b shows the PMCM resistance map of a tantalum-oxide-based memristor (see Experimental Section

© 2011 WILEY-VCH Verlag GmbH & Co. KGaA, Weinheim

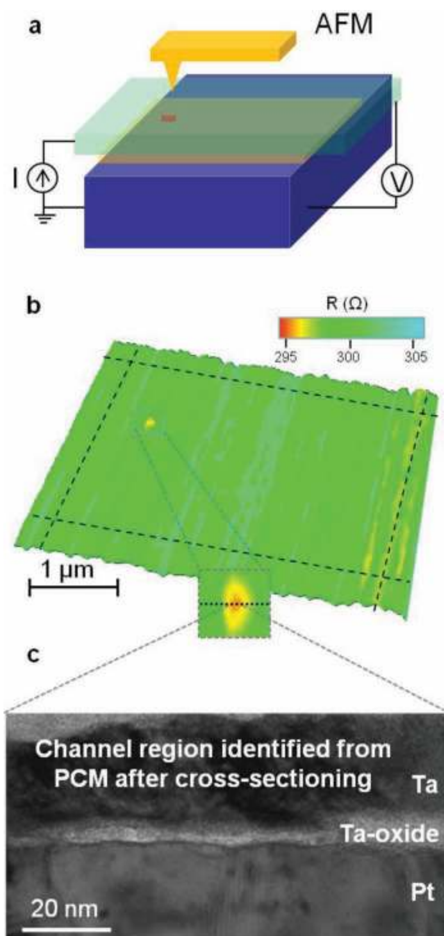

Figure 2. Identification and visualization of the conduction channel. a) Schematic illustration of PMCM, for which a non-conducting AFM tip applied pressure to the top electrode while the resistance of the device was monitored, yielding a resistance map as a function of tip position. b) The resistance map of a TaO_x-based memristor, where the red dot (resistance decrease), highlighted by the dashed square in the magnified inset, corresponds to the conduction channel. The color scale represents the measured resistance values. The conduction channel was cross-sectioned by FIB across the center (indicated by the black dashed line in the inset). c) TEM image of the conduction channel region identified from PMCM.

for details) in a low resistance state (ON state). On the resistance map, only one resistance dip of approximately 100 nm diameter (yellow–red dot) was observed, revealing that only one active switching region existed or was dominant in this device. Once the active switching region was located by PMCM, a dual beam FIB/scanning electron microscope was used to cross-section it, using careful registration to the PMCM map in order to cut across the identified channel. A TEM image of the resulting cross-section that includes the channel region is shown in Figure 2c. The structure and elemental composition of this area were then analyzed in detail.

Figure 3 shows the complete physical characterization of the conduction channel region from electron microscopy, spectroscopy, and diffraction (Figure 3a–e), and focused X-ray analysis from a synchrotron on a separate device (Figure 3f). Performing dark-field imaging around the location of the channel, a 5 nm nanocrystal was observed in Figure 3a. As grown, the tantalum oxide layer was amorphous and high-resolution TEM (HRTEM, Figure 3b) showed that the switching layer in the channel region remained amorphous throughout, except for this nanocrystal. To identify its composition and structure, convergent beam electron diffraction (CBED, bottom-left inset in Figure 3b) was performed and revealed only two intense diffraction spots corresponding to an interplanar spacing of 1.81 Å. We identified this structure as a base-centered monoclinic variant of a high-temperature (HT) tetragonal α-Ta_2O_5 phase.[58] While the above measured interplanar distance could also match that of β-Ta_2O_5 phase, the particular symmetry and extinction conditions, with only one set of strongly reflecting planes in the relevant zone, were more consistent with the HT α-Ta_2O_5 phase, as was corroborated by the diffraction simulation. The corresponding simulated (001) SAED (selected area electron diffraction), with diffracting 1.90 Å-spaced {020} planes, is shown in the right-bottom inset in Figure 3b. This phase is obtained by distortion of the HT α-Ta_2O_5 phase,[58] and the transformation from a low-temperature (LT) orthorhombic β-Ta_2O_5 to the HT tetragonal α-Ta_2O_5 phase[58] requires a temperature of 1633 K in bulk samples.[59,60] While much lower temperatures were likely required for crystallization from the as-grown, nanoscale amorphous TaO_x film, this still suggests that a relatively high temperature was attained in this localized region. Thus the presence of the insulating nanocrystal provides evidence of significant heating during the electrical operation, most likely caused by Joule heating from a nearby conduction channel, which makes temperature an important component of the switching mechanism. In addition, the known stoichiometric composition of the crystallite provides a good internal calibration for determining the Ta to O ratio around the channel region.

EELS was used to study the elemental composition around the channel region of Figure 3c. Horizontal and vertical line scans were collected, as indicated by the dashed lines, with the corresponding oxygen profiles shown in Figure 3d,e. By comparing this to the oxygen signal in a region of the device far away from the channel region (dashed black line of Figure 3e labeled "pristine"), it is clear that the oxygen content significantly decreased with lateral position from the Ta_2O_5 nanocrystal toward the center of the channel region, and the oxygen content inside the channel region was less than one third of that in the pristine film or the nanocrystal. Thus, the conduction channel consisted of Ta(O) solid solution and was amorphous (Figure 3b). This is in contrast to the crystalline conduction channels (Magneli Ti_4O_7) found in the titanium oxide system,[46,54] which has a significantly more complex phase diagram. As shown in Figure 3d,e, there was a distinct horizontal oxygen gradient and a much less pronounced vertical oxygen gradient within the channel region. The oxygen content was surprisingly high in the boundary region between the crystal and the conduction channel, as shown by the yellow dashed scan line in Figure 3c,e in addition to Figure 3d. In contrast, the Ta signal (not shown) did not show a significant variation.

Important complementary information on the nature of the conduction channel was recently provided by hard X-ray spectromicroscopy[61] (Figure 3f) performed on a Pt/TaO_x/Pt device, which exhibited similar switching behavior as the Pt/TaO_x/

© 2011 WILEY-VCH Verlag GmbH & Co. KGaA, Weinheim

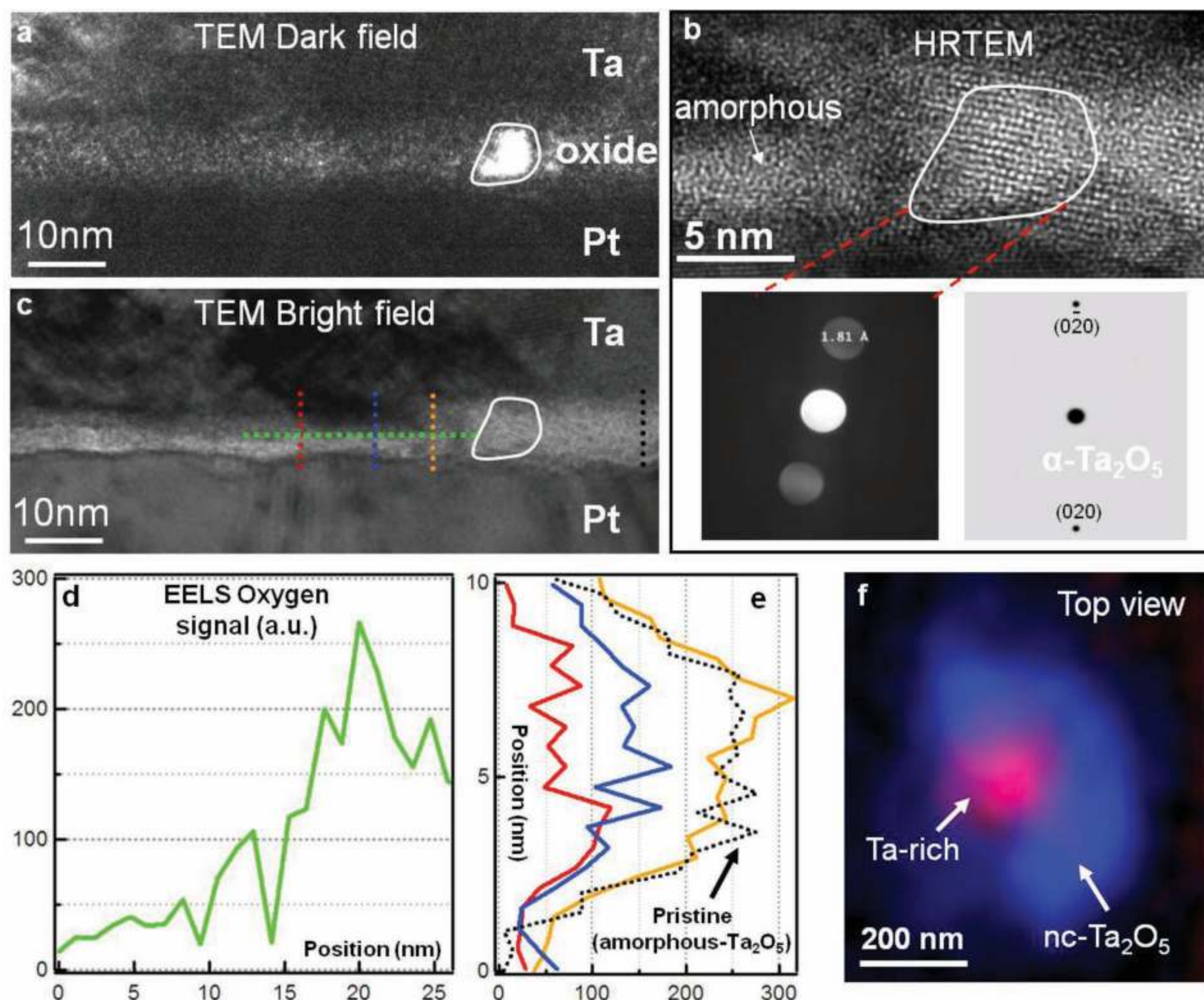

Figure 3. Structural and compositional analysis by electron microscopy, diffraction, and spectroscopy of the channel region identified in Figure 2. a) Dark-field imaging of the switching region showed a crystalline grain adjacent to the channel. SAED in the area provided several diffraction peaks that were selected for this dark-field image. b) HRTEM revealed a lattice pattern from a ≈5 nm nanocrystal, with the surrounding oxide being amorphous. CBED (bottom left) was taken within the nanocrystal and indexed by simulation (bottom right) to be α-Ta_2O_5. c) Bright-field TEM of the channel region with dashed lines indicating where horizontal and vertical EELS line profiles were obtained. d,e) Horizontal and vertical line profiles, respectively, of the background subtracted, integrated oxygen K-edge jump height from EELS, which is proportional to the oxygen atomic concentration. Horizontal profile (d) was collected across the border of the crystal and the channel region, showing a high oxygen concentration in the border region. Several vertical profiles (e) were collected moving toward the central channel region away from the nanocrystal (white outline). The oxygen profile for the pristine tantalum oxide film is shown (dashed black curve) for comparison. f) Synchrotron based nanobeam X-ray fluorescence measurement of a similar tantalum oxide device showing a central Ta-rich channel, surrounded by a nanocrystalline Ta_2O_5 phase.

Ta devices. A Ta-rich region was identified in the center of the image in Figure 3f, which corresponded to the Ta(O) solid solution phase described above. Surrounding this Ta(O) phase was a differentiated Ta-oxide phase that, from analysis of the L-edge absorption spectrum, had an increased short-range order compared to the amorphous Ta_2O_5 film (outer gray region of image), but without any increased concentration of Ta, therefore matching the description of the crystalline HT α-Ta_2O_5 phase from TEM. While only one nanocrystal was found by TEM, the larger area and volume probed by X-ray microscopy suggests that more highly ordered and stoichiometric Ta_2O_5 in fact surrounded the channel. The dimension of the channel region (around 150 nm) revealed by hard X-ray spectromicroscopy was comparable to that observed by PMCM (Figure 2b). The higher energy used in the very first switching cycle due to the longer pulse duration (Figure 1a) combined with the initially different heat dissipation condition are responsible for the formation of the crystalline phases. The switching region in the subsequent switching cycles is then likely contained within the surrounding crystalline region because of the relatively low tolerance of off-stoichiometry of crystalline materials.

The compositional changes and transport properties of the conduction channel (Figure 3) were further studied by growing and analyzing similar amorphous tantalum oxide films with various oxygen concentrations. The resistivity and temperature coefficient of resistance (TCR) of the films were

© 2011 WILEY-VCH Verlag GmbH & Co. KGaA, Weinheim

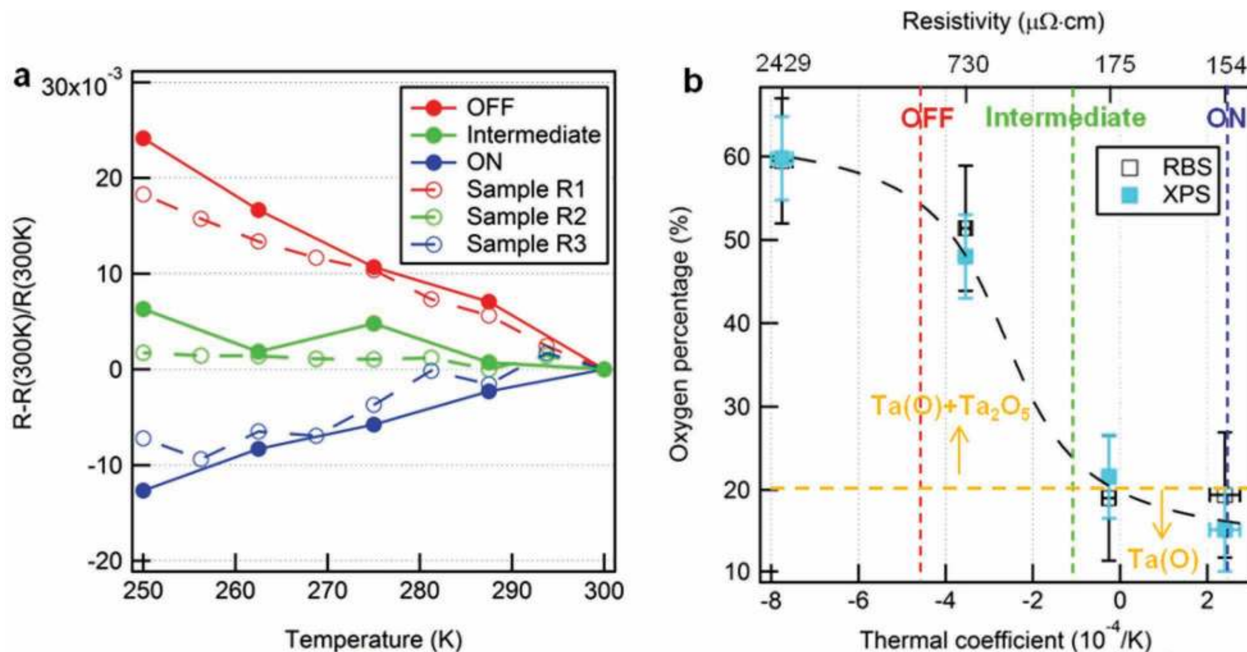

Figure 4. Comparison of the TCR between different memristor states and corresponding tantalum oxide calibration samples. a) Resistance change, normalized to 300 K, as a function of temperature for three different memristor states and reference thin films with varying oxygen concentration. b) Atomic oxygen percentage measured using RBS and XPS for the reference layers as a function of thermal coefficient of resistivity (bottom) and resistivity of the reference thin films (top). Black dashed curve is a guide to the eye. Horizontal yellow dashed line at 20% indicates the oxygen solubility limit in Ta thin films. Oxygen composition of the conduction channel for the three memristor states can be estimated using the TCR, as indicated by vertical dashed lines.

measured using a standard van der Pauw configuration, while the tantalum and oxygen compositions were measured by both Rutherford backscattering spectrometry (RBS) and in situ X-ray photoemission spectroscopy (XPS, see Experimental Section for details). As shown in **Figure 4**a,b, with increasing oxygen content in the films, the TCR of the Ta-O thin films decreased from a positive value to zero and then to a negative value (from metallic to nonmetallic behavior), closely matching the different memristor states (ON, intermediate, and OFF) both in the temperature dependence of the resistance (Figure 4a), and therefore the conduction mechanism, and in the resistance ratios between states. Based on matching the TCR of the reference films (shown in Figure 4b) and using the corresponding compositions obtained by XPS (also confirmed by RBS results), we can deduce the effective oxygen composition of the conduction channel to be approximately 15 ± 5 at% for the ON state, 23 ± 5 at% for the intermediate state, and 54 ± 5 at% for the OFF state, in good agreement with the EELS results. Thus, the resistance states of the device are well described by the strong dependence of the resistivity on the composition of the amorphous Ta(O) conduction channel and characterized by a transition from metallic to nonmetallic behavior.[62] In the low resistance state (ON state), the oxide has a lower oxygen concentration and exhibits metallic behavior, as seen by the linear current–voltage (I–V) curve in the ON state (Figure 1c) and the positive TCR (solid blue in Figure 4a). The OFF state has an almost linear I–V curve with a much smaller slope, but with a negative TCR. Thus, the ON/OFF resistance change should be caused by the modulation of the channel, either its shape or composition, rather than the variation of a tunnel gap as found for other switching oxides.[5,13,63] The absence of a tunnel gap between the metal electrode and conduction channel arises from the nature of the revealed conductance channel, which is a solid solution of oxygen in Ta and can thus form a metal (channel)/metal (electrode) wetting interface between the electrode and the channel that resists the insertion of an insulating oxide. A change in the channel radius should not significantly change the TCR, which is not strongly dependent on geometry, between different resistance states. Thus, the large TCR changes, both in magnitude and sign, from ON to intermediate to OFF state show that the composition change in the channel, rather than a radial or axial shape change, is the primary mechanism for the switching of Figure 1. Due to the destructiveness of the cross-sectioning, only one state of the device (ON) was studied in Figure 3, but based on the above, we expect the microscopic character of the conduction channel to be qualitatively similar to Figure 3 in the OFF state with a quantitative change in oxygen composition.

The addition of oxygen in the conduction channel to modulate the resistance state can be further understood as follows. The two stable phases of the Ta-O bulk system in equilibrium are insulating Ta_2O_5 and conductive Ta(O) solid solution, which may accommodate up to 20% oxygen based on atomic composition.[64] When the oxygen composition goes above the solubility limit in an amorphous thin film (indicated by the horizontal orange dashed line in Figure 4b), the Ta^{5+} oxidation state starts to appear as observed by XPS[62] and hopping conduction gradually becomes the dominant electron

© 2011 WILEY-VCH Verlag GmbH & Co. KGaA, Weinheim

transport mechanism, which coincides with an increasingly negative TCR. This transition from metal to Fermi glass behavior[62] appears to be the mechanism for OFF switching. Even though heating is substantial, the conduction channel remains amorphous, in contrast to the crystalline conduction channel in TiO_2 unipolar[46] and bipolar switches,[54] which is likely a result of off-stoichiometry of the conduction channel in the TaO_x memristor. The amorphous structure enables a significant mobile species accommodation capability for a continuous composition change and very high endurance switching. In the amorphous channel, it is the motion of oxygen anions rather than oxygen vacancies (as in the crystalline Ti_4O_7 channel) responsible for the switching. The higher oxygen concentration observed in the boundary region between conduction channel and the crystallite (Figure 3c–e) suggests a lateral (annular) oxygen reservoir in parallel to the channel. The observed vertical oxygen concentration gradient is formed by the electric field while the more significant lateral oxygen gradient should be caused by thermal effects (Figure 3d,e). Therefore, the motion of oxygen anions is both vertical and lateral in the switching as a combined result of both electric field and thermal effect. An oxygen vacancy reservoir is necessarily more conductive than the channel region and therefore can only be in series with the channel, such as those found in Ti-O memristors.[46,54] In this case, Fick diffusion (thermal effect) always tends to push more oxygen vacancies into the tunnel gap vertically and make the OFF switching harder and slower. In Ti-O memristors, the OFF switching can be slower than ON switching by orders of magnitude for the same applied absolute voltage due to the fact that Fick diffusion and drift drive the mobile species in opposite directions during the OFF switching.[63,65] However, for the Ta-O memristor with a lateral oxygen reservoir, the Fick diffusion tends to push oxygen ions into the conduction channel laterally and facilitate the OFF switching. This may explain the observation in Figure 1a, where, in contrast to the Ti-O memristor, the device can be switched OFF at sub-2 ns speed with a small voltage. Since Joule heating in memristors may be unavoidable and even necessary for obtaining both fast switching and long state retention times, the parallel configuration of the reservoir is superior to a series configuration because the former can cooperatively utilize the heating effect with electric field. This further enables a much lower operation energy for Ta-O type devices, as shown in Figure 1c, where a less than 10   A current is used to switch a 50 nm × 50 nm device as compared with over 100   A for a similar size Ti-O nanodevice.[13]

While it is easy to understand how oxygen ions are driven in and out of the channel vertically by an electric field, there is no generally accepted theory to explain the lateral motion of oxygen ions in and out of the channel. One possible rationalization of the experimental observation is that Fick diffusion tends to drive oxygen ions in while thermophoresis[66,67] tends to drive oxygen ions out. Fick diffusion dominates over thermophoresis during the OFF switching, where the higher electrical and thermal conductivity of the ON state channel distributes the heat more uniformly as power is applied to the device and the resulting temperature gradient is flatter. Thermophoresis dominates during the ON switching, where a steep radial temperature gradient is produced by Joule (I^2R where I is current and R is resistance) heating in the high-resistance OFF state with poor thermal conductivity.

Based on the above results and properties of the Ta-O system, we can now infer criteria for selecting other high-speed, high-endurance, and low-energy memristors. A simple binary system is preferable, with only two thermodynamically stable phases in equilibrium, one insulating and the other conducting. The reliability of the memristor is directly linked to the absence of intermediate phases that could form in the conduction channel during the switching process. The Hf-O system also meets these requirements and is the only other system so far reported to have exhibited an endurance close to 10 billion.[68]

In conclusion, a precise approach to locate and directly image the key switching component was demonstrated on Ta oxide memristors that exhibited excellent electrical performance in many categories. The nanoscale area responsible for the switching was found to consist of an amorphous Ta(O) solid solution, surrounded by a stoichiometric and nanocrystalline Ta_2O_5. Together with the temperature dependent transport properties for various device states and reference films, we argue that the switching observed here is the result of a composition modulation (oxygen concentration) of a conduction channel in parallel with a reservoir by the cooperative combination of thermal and electric field effects. The microscopic mechanism of switching revealed by the detailed structure, composition, and electrical behavior of the conduction channel is key to engineering further improvements in the devices.

Experimental Section

The TaO_x film of the devices was sputtered from a tantalum oxide target (nominal composition to be Ta_2O_5) with an Ar gas pressure of about 3 mTorr. The device substrate was 200 nm SiO_2 on Si wafer. The disc device stack consisted of (from bottom to top) 1 nm Ti blanket adhesion layer, 100–400 nm Pt blanket bottom electrode, 18 nm tantalum oxide blanket layer, and 100–400 nm Ta disc (100   m diameter) top electrode. Metallic Pt and Ti layers were deposited by electron-beam evaporation at ambient temperature and the metallic Ta layer was DC sputter-deposited at ambient temperature. The 50 nm × 50 nm nanojunction was patterned by ultraviolet nanoimprint lithography with a stack structure of Si/SiO_2 200 nm/Ta 2 nm/Pt 9 nm/TaO_x 8 nm/Ta 11 nm/Pt 2 nm.

Current–voltage switching curves and resistance measurements were performed using an Agilent B1500A parameter analyzer. A Veeco Multimode AFM was used for PMCM. A careful comparison between AFM contact/tapping mode images and SEM (FEI XL30) images was used for the registration of the conduction channel located by PMCM and cross-sectioned by a dual-beam SEM/FIB.

The reference tantalum oxide films (100–200 nm on a substrate of 110 nm SiO_2 on Si wafer) were radio frequency (RF)-sputtered from a Ta target in an AJA International, Inc. magnetron sputtering system, with 150 W at a dynamic pressure 8 mTorr, Ar flow rate 20 sccm (standard cubic centimeters per minute) and O_2 flow rate varying from 0.5 to 0 sccm (R0, with the highest oxygen percentage in Figure 4c: 0.5 sccm; R1: 0.25 sccm; R2: 0 sccm; R3: 0 sccm with high-temperature annealing). The vacuum of the chamber before gas introduction was ≈2 × 10^{-8} mbar. The substrate temperature during the deposition was held at ≈700 K. Measurement of the TCR was done in a Janis cryostat, with the temperature ramped both up and down between 250 K and 300 K in nine steps with equal intervals. Square-shaped (5 mm × 5 mm) samples of tantalum oxide reference films with contact pads (10 nm Ti covered by 30 nm Pt) at the corners were used for the resistivity measurements in a van der Pauw configuration.

© 2011 WILEY-VCH Verlag GmbH & Co. KGaA, Weinheim

Sample thickness and average composition were obtained from RBS by Evans Analytical Group, which showed a uniform composition profile for the whole film thickness. The oxygen percentage of the films was also determined from a weighted sum using the oxidation state extracted by 4f core-level XPS. The XPS measurements were done following layer deposition in an in-situ analysis chamber with 6×10^{-10} mbar base pressure, employing a monochromated Al anode (1486.7 eV) and EIS-SPHERA hemispherical analyzer by Omicron Nanotechnology, GmbH.

HRTEM and CBED measurements were performed after cross-sectioning using a JEOL 2500SE at 200 keV. EELS was performed using an FEI Titan model 80–300 with an electron energy of 300 keV. EELS profiles 10 to 30 nm in length were acquired at several locations within the cross-sectioned device, using a far away profile roughly 1 m away for reference of the pristine film. Simultaneous EDS measurements were performed along with the EELS, and drifting was compensated using periodic reference images during the measurements.

X-ray measurements of Figure 3f were acquired at the Advanced Photon Source, Hard X-ray Nanoprobe beamline. A Fresnel zone plate focused the X-rays to a ≈70 nm full width at half-maximum spot size at the sample. X-rays were incident nearly perpendicular to the plane of the sample while scanned laterally using an optomechanical nanopositioning system based on laser doppler interferometry. The element-specific fluorescence was detected at each point in the scan using a four-element silicon drift energy dispersive detector, which allowed simultaneous mapping of the different material components in the device as well as more detailed material information by sweeping the incident X-ray energy. The photon energy was scanned around the Ta L_3 absorption edge (≈10 keV) to probe the tantalum oxide layer with a fine structure in the spectrum that is sensitive to microscopic structure, valence state, and chemical bonding information. The probing depth of the X-rays and emitted fluorescence was longer than the thickness of the entire device material stack. For the X-ray experiments, a top electrode of Pt was used rather than Ta so that all signal from the Ta L_3 edge is known to arise from the switching layer, rather than the electrode. For a Pt top electrode device, a stronger forming step was required, but no apparent differences in the behavior in terms of current–voltage shape during switching were observed between these two types of devices, suggesting a similar mechanism and structure for the conduction channel. Figure 3f is a composite of two analyses: 1) post-edge (9985 eV) information which images Ta concentration levels, shown by red coloring and 2) the white line (9885–9893 eV) intensity showing fine structure indicative of a change in the short range order (crystallinity) and valence state, shown by the blue coloring.

Acknowledgements

F.M., J.P.S., and J.J.Y. contributed equally to this work. The authors thank Matthew D. Pickett and Wei Yi for valuable discussions; they thank Xuema Li, T. Ha, C. Le, Martin Holt, Volker Rose, and Sujing Xie for excellent experimental assistance. The work at HP was sponsored by the U.S. Government's Nano-Enabled Technology Initiative. The use of the Advanced Photon Source and the Center for Nanoscale Materials was supported by the U.S. Department of Energy, Office of Science, Office of Basic Energy Sciences, under Contract DE-AC02-06CH11357.

Received: September 1, 2011
Revised: September 23, 2011
Published online: November 8, 2011

[1] J. H. M. Garner, Workshop & ERD/ERM Working Group Meeting (April 6-7, 2010) http://www.itrs.net/Links/2010ITRS/2010Update/ToPost/ERD_ERM_2010FINALReportMemoryAssessment_ITRS.pdf (accessed Septermber 2011).
[2] E. M. Vogel, *Nat. Nanotechnol.* **2007**, *2*, 25.
[3] A. Chung, J. Deen, J. S. Lee, M. Meyyappan, *Nanotechnology* **2010**, *21*, 412001.
[4] R. Waser, M. Aono, *Nat. Mater.* **2007**, *6*, 833.
[5] R. Waser, R. Dittmann, G. Staikov, K. Szot, *Adv. Mater.* **2009**, *21*, 2632.
[6] A. Sawa, *Mater. Today* **2008**, *11*, 28.
[7] Y. V. Pershin, M. Di Ventra, *Adv. Phys.* **2011**, *60*, 145.
[8] M. Hosomi, H. Yamagishi, T. Yamamoto, K. Bessho, Y. Higo, K. Yamane, H. Yamada, M. Shoji, H. Hachino, C. Fukumoto, H. Nagao, H. Kano, in *IEEE Int. Electron Device Meeting 2005, Tech. Dig.* IEEE, New York **2005**, p. 473.
[9] S. S. P. Parkin, C. Kaiser, A. Panchula, P. M. Rice, B. Hughes, M. Samant, S. H. Yang, *Nat. Mater.* **2004**, *3*, 862.
[10] L. O. Chua, *IEEE Trans. Circuit Theory* **1971**, *CT-18*, 507.
[11] L. O. Chua, S. M. Kang, *Proc. IEEE* **1976**, *64*, 209.
[12] D. B. Strukov, G. S. Snider, D. R. Stewart, R. S. Williams, *Nature* **2008**, *453*, 80.
[13] J. J. Yang, M. D. Pickett, X. Li, D. A. A. Ohlberg, D. R. Stewart, R. S. Williams, *Nat. Nanotechnol.* **2008**, *3*, 429.
[14] L. O. Chua, *Appl. Phys. A* **2011**, *102*, 765.
[15] M. Di Ventra, Y. V. Pershin, L. O. Chua, *Proc. IEEE* **2009**, *97*, 1717.
[16] J. Yao, Z. Sun, L. Zhong, D. Natelson, J. M. Tour, *Nano Lett.* **2010**, *10*, 4105.
[17] K. Szot, W. Speier, G. Bihlmayer, R. Waser, *Nat. Mater.* **2006**, *5*, 312.
[18] S. C. Chae, J. S. Lee, S. Kim, S. B. Lee, S. H. Chang, C. Liu, B. Kahng, H. Shin, D. W. Kim, C. U. Jung, S. Seo, M. J. Lee, T. W. Noh, *Adv. Mater.* **2008**, *20*, 1154.
[19] C. Schindler, M. Weides, M. N. Kozicki, R. Waser, *Appl. Phys. Lett.* **2008**, *92*, 122910.
[20] M. N. Kozicki, M. Park, M. Mitkova, *IEEE Trans. Nanotechnol.* **2005**, *4*, 331.
[21] M. N. Kozicki, C. Gopalan, M. Balakrishnan, M. Mitkova, *IEEE Trans. Nanotechnol.* **2006**, *5*, 535.
[22] B. J. Choi, D. S. Jeong, S. K. Kim, C. Rohde, S. Choi, J. H. Oh, H. J. Kim, C. S. Hwang, K. Szot, R. Waser, B. Reichenberg, S. Tiedke, *J. Appl. Phys.* **2005**, *98*, 033715.
[23] K. M. Kim, S. J. Song, G. H. Kim, J. Y. Seok, M. H. Lee, J. H. Yoon, J. Park, C. S. Hwang, *Adv. Funct. Mater.* **2011**, *21*, 1587.
[24] R. L. McCreery, J. Wu, R. P. Kalakodimi, *Phys. Chem. Chem. Phys.* **2006**, *8*, 2572.
[25] H. K. Yoo, S. B. Lee, J. S. Lee, S. H. Chang, M. J. Yoon, Y. S. Kim, B. S. Kang, M. J. Lee, C. J. Kim, B. Kahng, T. W. Noh, *Appl. Phys. Lett.* **2011**, *98*, 183507.
[26] S. H. Jo, K. H. Kim, W. Lu, *Nano Lett.* **2009**, *9*, 496.
[27] S. H. Jo, T. Chang, I. Ebong, B. B. Bhadviya, P. Mazumder, W. Lu, *Nano Lett.* **2010**, *10*, 1297.
[28] J. Yao, L. Zhong, Z. X. Zhang, T. He, Z. Jin, P. J. Wheeler, D. Natelson, J. M. Tour, *Small* **2009**, *5*, 2910.
[29] Z. Wei, Y. Kanzawa, K. Arita, Y. Katoh, K. Kawai, S. Muraoka, S. Mitani, S. Fujii, K. Katayama, M. Iijima, T. Mikawa, T. Ninomiya, R. Miyanaga, Y. Kawashima, K. Tsuji, A. Himeno, T. Okada, R. Azuma, K. Shimakawa, H. Sugaya, I. Takagi, R. Yasuhara, K. Horiba, H. Kumigashira, M. Oshima, in *IEEE Int. Electron Devices Meeting 2008, Tech. Dig.* IEEE, New York **2008**, p. 293.
[30] K. Terabe, T. Hasegawa, T. Nakayama, M. Aono, *Nature* **2005**, *433*, 47.
[31] E. Linn, R. Rosezin, C. Kugeler, R. Waser, *Nat. Mater.* **2010**, *9*, 403.
[32] M. Janousch, G. I. Meijer, U. Staub, B. Delley, S. F. Karg, B. P. Andreasson, *Adv. Mater.* **2007**, *19*, 2232.
[33] I. H. Inoue, S. Yasuda, H. Akinaga, H. Takagi, *Phys. Rev. B* **2008**, *77*, 035105.
[34] M. J. Rozenberg, I. H. Inoue, M. J. Sanchez, *Phys. Rev. Lett.* **2004**, *92*, 178302.
[35] J. R. Jameson, *Appl. Phys. Lett.* **2007**, *91*, 112101.
[36] Y. B. Nian, J. Strozier, N. J. Wu, X. Chen, A. Ignatiev, *Phys. Rev. Lett.* **2007**, *98*, 146403.

© 2011 WILEY-VCH Verlag GmbH & Co. KGaA, Weinheim

[37] S. Q. Liu, N. J. Wu, A. Ignatiev, *Appl. Phys. Lett.* **2000**, *76*, 2749.
[38] G. Yang, H.-Y. Chen, L. Ma, Y. Shao, Y. Yang, *Appl. Phys. Lett.* **2009**, *95*, 203506.
[39] J. Yao, L. Zhong, D. Natelson, J. M. Tour, *J. Am. Chem. Soc.* **2011**, *133*, 941.
[40] J. Borghetti, G. S. Snider, P. J. Kuekes, J. J. Yang, D. R. Stewart, R. S. Williams, *Nature* **2010**, *464*, 873.
[41] T. Hasegawa, T. Ohno, K. Terabe, T. Tsuruoka, T. Nakayama, J. K. Gimzewski, M. Aono, *Adv. Mater.* **2010**, *22*, 1831.
[42] Q. F. Xia, W. Robinett, M. W. Cumbie, N. Banerjee, T. J. Cardinali, J. J. Yang, W. Wu, X. M. Li, W. M. Tong, D. B. Strukov, G. S. Snider, G. Medeiros-Ribeiro, R. S. Williams, *Nano Lett.* **2009**, *9*, 3640.
[43] J. J. Yang, M. X. Zhang, J. P. Strachan, F. Miao, M. D. Pickett, R. D. Kelley, G. Medeiros-Ribeiro, R. S. Williams, *Appl. Phys. Lett.* **2010**, *97*, 232102.
[44] W. Yi, F. Perner, M. Qureshi, H. Abdalla, M. Pickett, J. Yang, M.-X. Zhang, G. Medeiros-Ribeiro, R. Williams, *Appl. Phys. A* **2011**, *102*, 973.
[45] M.-J. Lee, C. B. Lee, D. Lee, S. R. Lee, M. Chang, J. H. Hur, Y.-B. Kim, C.-J. Kim, D. H. Seo, S. Seo, U. I. Chung, I.-K. Yoo, K. Kim, *Nat. Mater.* **2011**, *10*, 625.
[46] D. H. Kwon, K. M. Kim, J. H. Jang, J. M. Jeon, M. H. Lee, G. H. Kim, X. S. Li, G. S. Park, B. Lee, S. Han, M. Kim, C. S. Hwang, *Nat. Nanotechnol.* **2010**, *5*, 148.
[47] J. J. Yang, N. P. Kobayashi, J. P. Strachan, M. X. Zhang, D. A. A. Ohlberg, M. D. Pickett, Z. Li, G. Medeiros-Ribeiro, R. S. Williams, *Chem. Mater.* **2011**, *23*, 123.
[48] J. J. Yang, J. Strachan, F. Miao, M.-X. Zhang, M. Pickett, W. Yi, D. Ohlberg, G. Medeiros-Ribeiro, R. Williams, *Appl. Phys. A* **2011**, *102*, 785.
[49] J. H. Hur, M.-J. Lee, C. B. Lee, Y.-B. Kim, C.-J. Kim, *Phys. Rev. B* **2010**, *82*, 155321.
[50] G. Dearnaley, A. M. Stoneham, D. V. Morgan, *Rep. Prog. Phys.* **1970**, *33*, 1129.
[51] S. Ssenyange, H. J. Yan, R. L. McCreery, *Langmuir* **2006**, *22*, 10689.
[52] K. Suzuki, N. Igarashi, K. Kyuno, *Appl. Phys. Exp.* **2011**, *4*, 051801.
[53] Y. C. Yang, F. Pan, Q. Liu, M. Liu, F. Zeng, *Nano Lett.* **2009**, *9*, 1636.
[54] J. P. Strachan, M. D. Pickett, J. J. Yang, S. Aloni, A. L. David Kilcoyne, G. Medeiros-Ribeiro, R. Stanley Williams, *Adv. Mater.* **2010**, *22*, 3573.
[55] C. N. Lau, D. R. Stewart, R. S. Williams, M. Bockrath, *Nano Lett.* **2004**, *4*, 569.
[56] J. J. Yang, F. Miao, M. D. Pickett, D. A. A. Ohlberg, D. R. Stewart, C. N. Lau, R. S. Williams, *Nanotechnology* **2009**, *20*, 215201.
[57] F. Miao, J. J. Yang, J. P. Strachan, D. Stewart, R. S. Williams, C. N. Lau, *Appl. Phys. Lett.* **2009**, *95*, 113503.
[58] X. Q. Liu, X. D. Han, Z. Zhang, L. F. Ji, Y. J. Jiang, *Acta Mater.* **2007**, *55*, 2385.
[59] O. Yamaguchi, D. Tomihisa, T. Uegaki, K. Shimizu, *J. Am. Ceram. Soc.* **1987**, *70*, C335.
[60] S. Wu, H. M. Chan, M. P. Harmer, *J. Am. Ceram. Soc.* **2005**, *88*, 2369.
[61] J. P. Strachan, G. Medeiros-Ribeiro, J. J. Yang, M. X. Zhang, F. Miao, I. Goldfarb, M. Holt, V. Rose, R. S. Williams, *Appl. Phys. Lett.* **2011**, *98*, 242114.
[62] I. Goldfarb, F. Miao, J. J. Yang, W. Yi, J. P. Strachan, M.-X. Zhang, M. D. Pickett, G. Medeiros-Ribeiro, R. S. Williams, unpublished.
[63] M. D. Pickett, D. B. Strukov, J. L. Borghetti, J. J. Yang, G. S. Snider, D. R. Stewart, R. S. Williams, *J. Appl. Phys.* **2009**, *106*, 074508.
[64] D. Gerstenberg, C. J. Calbick, *J. Appl. Phys.* **1964**, *35*, 402.
[65] D. B. Strukov, J. L. Borghetti, R. S. Williams, *Small* **2009**, *5*, 1058.
[66] I. Goldhirsch, D. Ronis, *Phys. Rev. A* **1983**, *27*, 1616.
[67] L. J. T. M. Kempers, *J. Chem. Phys.* **2001**, *115*, 6330.
[68] H. Y. Lee, Y. S. Chen, P. S. Chen, P. Y. Gu, Y. Y. Hsu, S. M. Wang, W. H. Liu, C. H. Tsai, S. S. Sheu, P. C. Chiang, W. P. Lin, C. H. Lin, W. S. Chen, F. T. Chen, C. H. Lien, M. J. Tsai, in *2010 Int. Electron Devices Meeting - Techn. Dig.* IEEE, New York **2010**, p. 460.

© 2011 WILEY-VCH Verlag GmbH & Co. KGaA, Weinheim